JOURNAL OF MATERIALS SCIENCE 24 (1989) 658–670

Properties and microstructures of Lanxide® Al_2O_3–Al ceramic composite materials

M. K. AGHAJANIAN, N. H. MACMILLAN*, C. R. KENNEDY, S. J. LUSZCZ, R. ROY*
Lanxide Corporation, One Tralee Industrial Park, Newark, Delaware 19711, USA and
**Materials Research Laboratory, The Pennsylvania State University, University Park, Pennsylvania 16802, USA*

A study has been made of four Al_2O_3–Al composite materials fabricated by the directed oxidation of molten aluminium alloys. Their microstructures are described and measurements of density, coefficient of thermal expansion, thermal conductivity, hardness, elastic constants, compressive strength, flexural strength, fracture toughness, work of fracture, and thermal shock resistance are reported. Compared to a typical dense sintered Al_2O_3, such as Durafrax® 1542, which is somewhat harder, stiffer, and stronger in compression, the new composites can be stronger in flexure, particularly at high temperatures, far tougher, and considerably more resistant to thermal shock. Attempts are made to relate their differences in properties to microstructure.

1. Introduction

There has recently been a resurgence of interest in ceramics for a variety of structural applications, ranging from high-temperature gas turbines and adiabatic diesel engines to cutting tools and other wear-resistant parts. In each case the applications make use of the beneficial properties of ceramics, including high stiffness, strength and hardness, low density, and good resistance to corrosion, oxidation, wear, and high temperatures. In most structural applications, the primary disadvantage of ceramics is their lack of toughness, which renders them sensitive to sudden catastrophic failure in response to accidental overloading, contact damage, or rapid temperature changes. This has led to attempts to develop ceramic composites which provide the best possible toughness and thermal shock resistance without significant loss of other desirable properties.

A variety of stratagems has been adopted in the search for greater toughness [1–8]. These include incorporation of metallic and/or ceramic fibres and/or whiskers [9–14]; incorporation of more or less equiaxed second-phase particles, both ductile [15–22] and brittle [23–25]; control of grain size, porosity, or other microstructural features [26–35]; and transformation toughening by the incorporation of tetragonal ZrO_2 particles or, in the case of ZrO_2-based ceramics, by alloying to provide either a dispersion of metastable tetragonal particles in a cubic matrix or a wholly tetragonal material [36–40]. Second-phase particles can play a number of roles. They can deflect cracks out of their paths, cause them to bow between obstacles, cause them to bifurcate, or cause the nucleation of additional microcracks ahead of the primary crack [41–53].

The present work is concerned with establishing the mechanical and thermal shock behaviour of novel Al_2O_3–Al composites produced by oxidizing aluminium alloys [54] and relating these properties to microstructure. For purposes of comparison, parallel measurements on a typical dense sintered Al_2O_3 are also reported. It is demonstrated that the structures and properties of the new composites can be controlled by varying the growth parameters. Future papers will describe the use of the Al_2O_3–Al oxidation reaction and other similar reactions as a method for forming composite materials around ceramic filler materials, allowing further opportunities to modify the properties of the resulting composites.

2. Experimental materials: macrostructure and microstructure

The materials studied were four Al_2O_3–Al composites, hereinafter designated A, B, C and D, and Durafrax® 1542, a commercially available dense sintered Al_2O_3 (Sohio Engineered Materials Co., Niagara Falls, New York). The composites were typical of the monolithic materials now being grown in tens of kilogram sizes to thicknesses exceeding 20 cm by the process described in an earlier publication [54]. Material A was grown by oxidizing an aluminium alloy in air at 1400 K and stopping the growth before all of the metal had been converted to oxide. Material B was produced in the same fashion, but the process was allowed to run to completion. In a parallel manner, Material C was grown by incompletely oxidizing an aluminium alloy in air at 1600 K, and Material D was produced by letting this latter reaction proceed to completion. The structures and properties of Materials A and B are vastly different, while those of Materials C and D are quite similar. Hence, the present paper describes the structures of all four materials, but it only explores the properties of Materials A, B and D.

The microstructures, phase constitutions and

0022–2461/89 $03.00 + .12

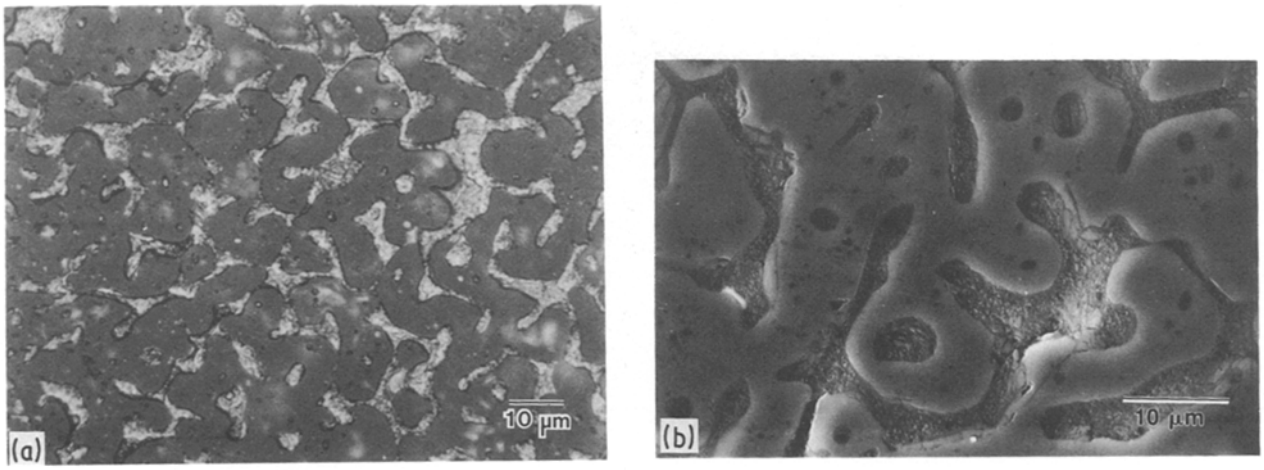

Figure 1 (a) Optical and (b) scanning electron micrographs showing reflected light and secondary electron images of a polished cross-section of Material A.

chemical compositions of the composites were studied by lineal analysis of ceramographically prepared cross-sections, wet chemical analysis, mercury porosimetry, BET surface area analysis [55], X-ray diffractometry, optical microscopy, scanning electron microscopy and transmission electron microscopy. All lineal analyses and microscopic investigations were conducted on surfaces oriented perpendicular to the growth direction. In addition, the densities of the composites were determined by pycnometry and/or weighing and measuring regularly shaped pieces, and measurements were made of their permeabilities to gas (N_2) and liquid (H_2O) in the growth direction. For present purposes it is sufficient to summarize just a few of the findings of these investigations.

The microstructures of the new composites are complex. X-ray diffraction and transmission electron microscopy show that they consist of an α-Al_2O_3 matrix containing various dispersions of aluminium alloy and/or pores.

Two experiments show that Material A (Figs 1a and b) is a 3 : 3 : 0 composite* [56]. First, repeated sectioning and polishing reveal that the Al_2O_3 and aluminium phases are both interconnected in all three dimensions; and second, the impermeability of the material to both N_2 and H_2O reveals that the porosity, a minor constituent, is not interconnected. Similar studies show that Material B (Fig. 2) is a 3 : 0 : 3 composite in which the Al_2O_3 is continuous in all three dimensions, the aluminium exists as isolated inclusions, and the network of pores is interconnected in all three dimensions. In the case of Material B(i) (see below) the resultant permeability to H_2O is $\sim 4 \times 10^{-5}$ darcy ($\equiv \sim 4 \times 10^{-17}\,m^2$) and the permeability to N_2, which varies with driving pressure, extrapolates to a similar value at infinite pressure.

Lineal analysis shows that the volume fractions of aluminium and porosity in Material A are 0.22 and 0.04, respectively, and that typical individual pores (none of which lie within the field of view in Figs 1a and b) are larger than the characteristic dimension of the microstructure. Fig. 1b shows that there is little or no porosity at the Al–Al_2O_3 interface. (The dark contrast visible at this interface in Fig. 1a is an artefact of the polishing procedure. Aluminium and Al_2O_3 differ greatly in hardness and this leads to the development of surface relief which can cause misleading contrast. The development of such relief has been suppressed in Fig. 1b by maintaining a high pressure on the specimen during polishing.) The volume fraction data are consistent with the results of wet chemical analysis, which reveal the aluminium content of the material to be 17 wt %.

Lineal analysis also shows that the volume fraction of Al_2O_3 in Material B varies widely with processing conditions. The present study investigated three Type B materials, hereinafter designated B(i), B(ii) and B(iii). These contain volume fractions of Al_2O_3 of 0.81, 0.74 and 0.72, respectively. From these figures and the measured densities (see Table I below) it can be calculated that the corresponding volume fractions of aluminium and porosity must be 0.03 and 0.16, 0.03 and 0.23, and 0.01 and 0.26, respectively.

In the case of Material B(ii), mercury porosimetry yielded a pore volume fraction of 0.20 ± 0.01, in reasonable agreement with the lineal analysis. In conjunction with the usual assumptions [55] that the mercury–specimen contact angle and surface tension are 140° and $0.485\,N\,m^{-1}$, respectively, the porosimetry studies also suggest that the characteristic pore dimension is of the order of one micrometre or less. These findings are in reasonable accord with the results of the BET surface area measurements, which yielded a surface area of $1.35 \times 10^3\,m^2\,kg^{-1}$ when krypton was used as the adsorbate. However, Fig. 2b shows that the pore size measurement is a gross underestimate. Either mercury wets material B(ii) in a manner very different from that assumed in the calibration of the porosimeter or the composite contains many "ink-bottle" pores (i.e. pores entered via a neck much smaller in diameter than the rest of the cavity). Two pieces of evidence support the latter contention. First, impregnating the sample with a 1 wt % solution of stearic acid in chloroform and then drying at 323 K for 20 min to coat the surface of the pores prior to mercury intrusion affected neither the measured pore size nor

*These numbers signify respectively the number of dimensions in which the Al_2O_3, aluminium, and pore regions are continuous.

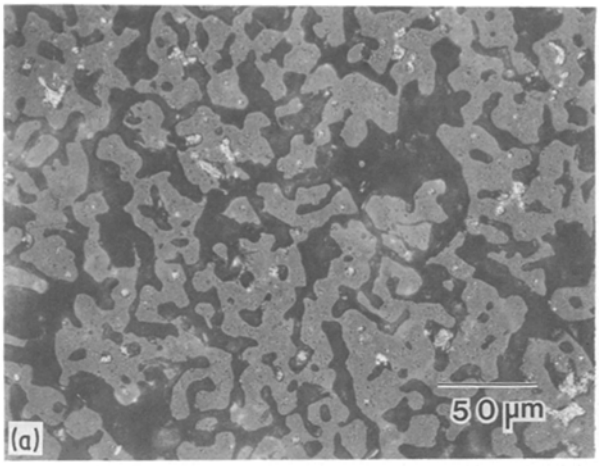

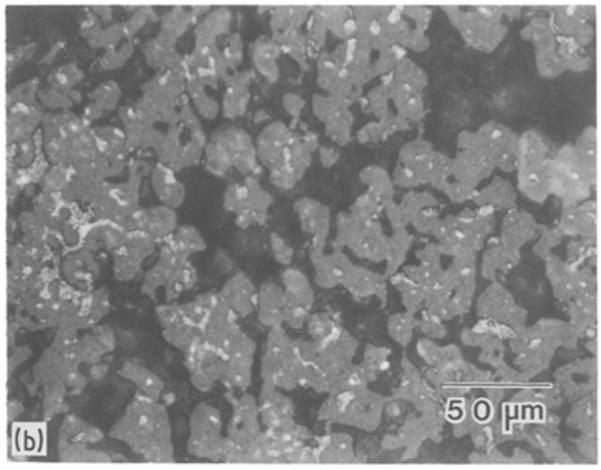

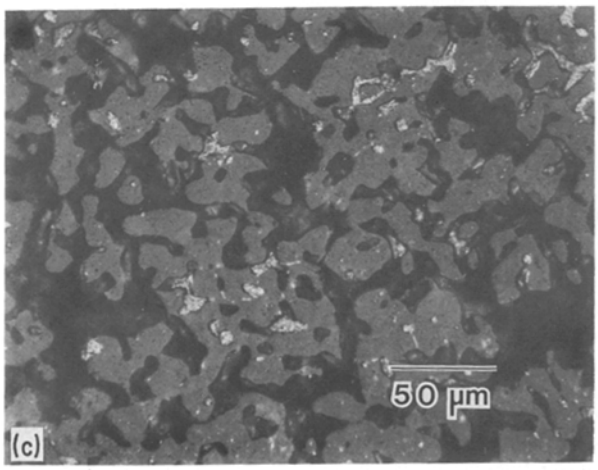

Figure 2 Optical micrographs showing reflected light images of polished cross-sections of Materials (a) B(i), (b) B(ii) and (c) B(iii).

the measured volume fraction of pore space. Second, the pores seen in Fig. 2 are tortuous in shape and exhibit many re-entrants, which factors are consistent with "ink-bottle" geometry and could also account for the relatively high surface area.

For Material B(ii) there is also reasonable agreement between the estimate of the weight fraction of aluminium obtained via lineal analysis and density measurement and that obtained from the weight gain during growth. For Material B(i), however, the observed weight gain during growth implies a higher aluminium content of about 8 wt %, and wet chemical analysis yielded an estimate of 9 wt % for the aluminium content of Material B(iii). These values are not in good agreement with the results of the lineal analyses and density measurements made on Materials B(i) and B(iii).

Materials C and D both exhibit a more or less regular hexagonal cellular macrostructure (Fig. 3). Inside the hexagonal cells both materials are identical 3:0:0 composites in which both the pores and the regions of aluminium alloy are isolated (Fig. 3d). The porosity is micrometre-scale and in these materials appears to occur in part at the Al–Al_2O_3 interface (Fig. 4). It is only in the vicinity of the cell walls that Materials C and D differ. In Material C the cell wall appears to contain relatively few (isolated) pores and both isolated and interconnected regions of alloy (Fig. 3b). Thus, this region has a microstructure midway between a 3:0:0 and a 3:2:0 composite. In Material D (Fig. 3c) the further progression of the growth process leads to an increase in the volume fraction of porosity along the cell wall (compare Figs 3b and c) and partial interconnection of the individual pores. In the limit, the cell wall region would become a 3:0:2 composite. However, in none of the materials studied in this work did the pores interconnect sufficiently to destroy their impermeability to either N_2 or H_2O. In both Materials C and D the pores in the cell walls typically have dimensions of a few micrometres or tens of micrometres.

The results of the lineal analyses and density determinations performed on Material C suggest that the volume fractions of aluminium alloy and porosity in this material are 0.16 and 0.03, respectively. The former figure is in good agreement with the estimate of 11 wt % Al obtained by wet chemical analysis. In Material D both volume fractions vary with reaction time. For those samples studied in this work, however, the values were held constant at 0.13 and 0.05, respectively.

In Materials A, C and D, the mean free paths* in the aluminium and Al_2O_3 phases are ~ 4 and $\sim 10\,\mu m$, respectively. In contrast, Material B has a somewhat coarser microstructure. Mean free paths of ~ 15, ~ 20 and $\sim 20\,\mu m$ were measured in the "pore phase" of Materials B(i), B(ii) and B(iii), respectively, and the corresponding figures for the Al_2O_3 phase are ~ 20, ~ 15 and $\sim 20\,\mu m$. It should be noted that the mean free path is much less variable in Materials C and D than in Materials A and B.

To date, extensive transmission electron microscopic investigations have only been carried out on Material A. These studies reveal that the grain size of the Al_2O_3 phase is $\geqslant 10\,\mu m$ and that each grain is divided into subgrains $\leqslant 1\,\mu m$ in size. The crystallographic misorientation between the subgrains is $\sim 1°$. The aluminium phase is also divided into subgrains $\leqslant 500$ nm in size which are separated by low-angle grain boundaries. Again the misorientation across the low-angle boundaries is $\sim 1°$. Higher-angle grain boundaries are also presumed to exist in the aluminium phase, but they must exist in fewer numbers – i.e. at larger

*Variously known as the mean linear intercept, particle size, interparticle distance or grain size, according to which of two (or more) phases is being considered and how the phases are interconnected. See Exner and Hougardy [57] for a detailed exposition.

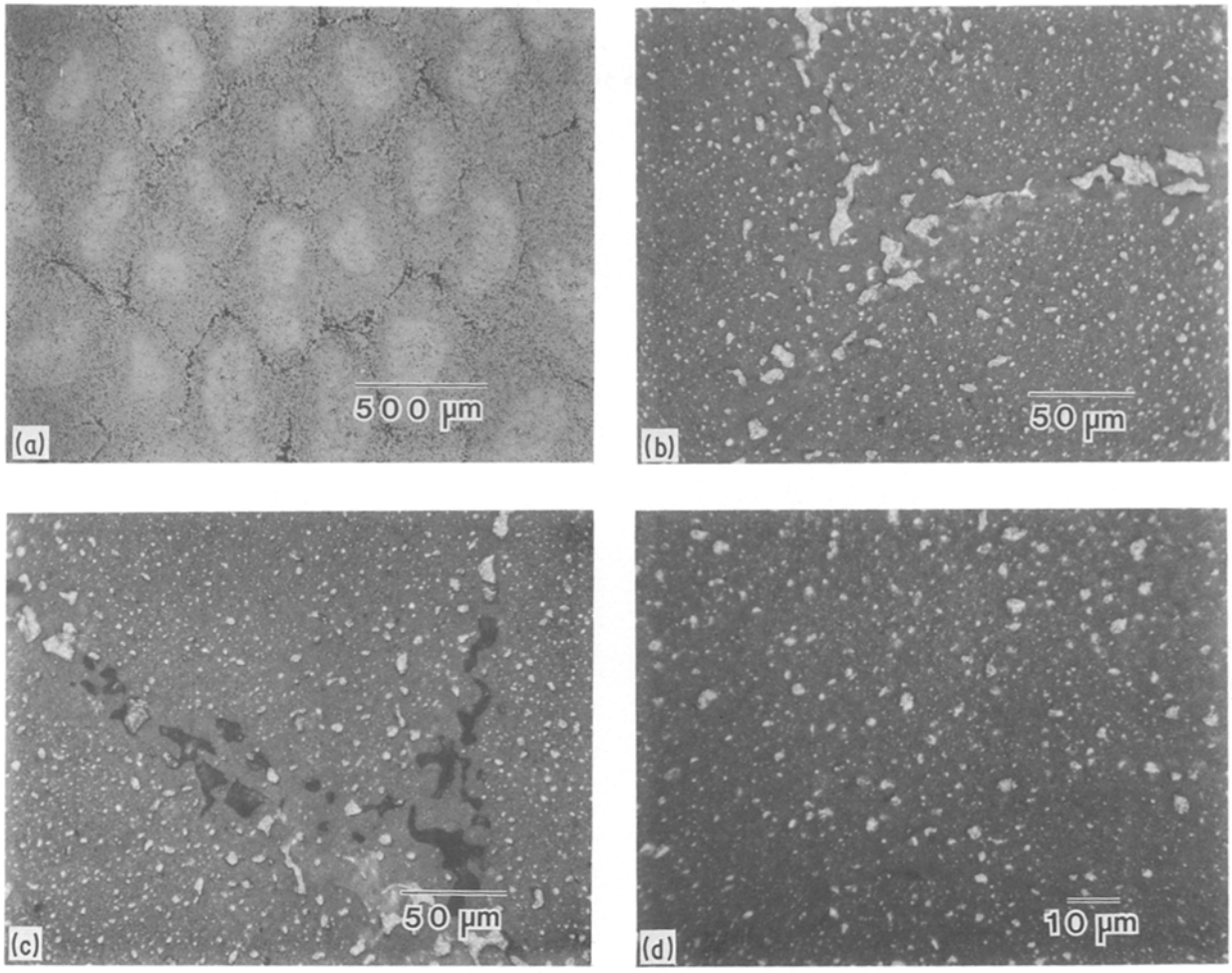

Figure 3 Optical micrographs showing reflected light images of polished cross-sections of (b) Material C and (a, c, d) Material D.

separations – because they have not yet been found in any of the thin foils examined. An important feature of the growth process is that it produces grain boundaries free of the low melting-point films that lead to loss of strength at high temperatures. Fig. 5 shows a "triple point" where an aluminium region meets two Al_2O_3 subgrains separated by a low-angle grain boundary. Note that both this boundary and the high-angle Al–Al_2O_3 phase boundary are sharply defined and free of any boundary layers more than ~10 nm in thickness. Higher-magnification micrographs of individual boundaries show no evidence of any such layer.

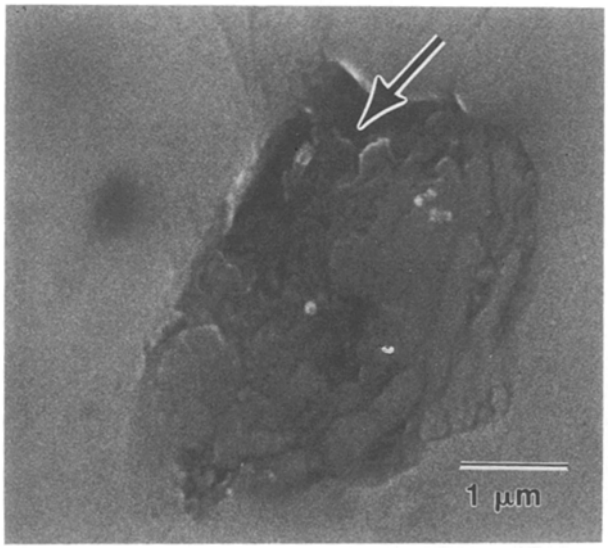

Figure 4 Scanning electron micrograph showing a secondary electron image of an inclusion of aluminium in Material D. Arrow indicates porosity at the Al–Al_2O_3 interface.

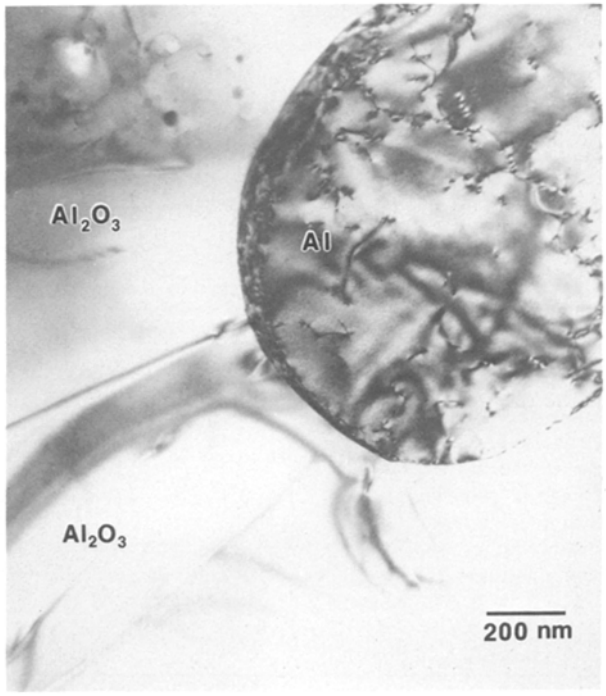

Figure 5 Bright-field transmission electron micrograph showing a low-angle Al_2O_3–Al_2O_3 grain boundary and a high-angle Al–Al_2O_3 phase boundary in Material A.

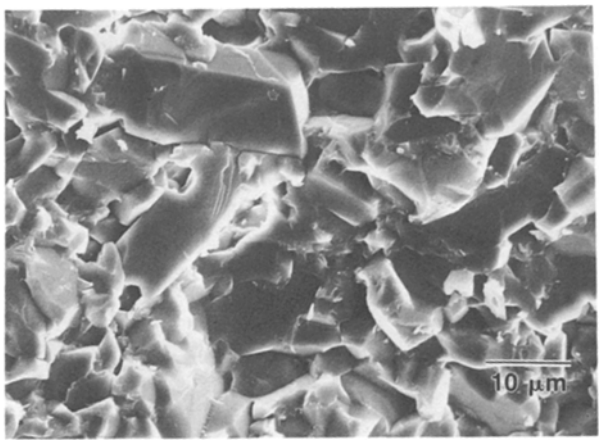

Figure 6 Scanning electron micrograph showing a secondary electron image of a fracture surface of Durafrax® 1542.

The microstructure of Durafrax® 1542 is seen most clearly in a fracture surface such as that shown in Fig. 6, which comes from the tensile side of a broken bend bar. This shows that the grain size is 5 to 10 μm and that the mode of fracture is primarily intergranular. The Al_2O_3 content of this material is 96 wt %, and there is an SiO_2-based glassy phase at the grain boundaries. Lineal analysis of polished cross-sections reveals that the volume fraction of porosity is ~ 0.05 and that the material is isotropic.

3. Results: mechanical and physical properties

Table I compares various mechanical and physical properties of Materials A, B and D with the corresponding properties of Durafrax® 1542. Where the data are sufficiently numerous both the mean value and the standard deviation are quoted. The thermal expansion α was measured perpendicular to the growth direction over the temperature range 300 to 1300 K with a Harrop TD-716 thermal dilatometer, and the thermal conductivity k was measured parallel to the growth direction using a Colora thermoconductometer which found the average over the temperature interval 360 to 373 K. Young's modulus E was measured at room temperature by the sonic resonance (standing wave) technique [58], using flexural and longitudinal modes of vibration of a bar oriented perpendicular to the growth direction; and the shear modulus G was determined by applying the torsional variation of the same technique to the same specimen. Poisson's ratio was then calculated as $\nu = (E/2G) - 1$. The Vickers hardness was measured on surfaces oriented perpendicular to the growth direction with a Leitz Miniload hardness tester, using a loading time of 10 sec. Values representative of the composite were obtained using a load of 20 N, which produced an indentation large compared to the scale of the microstructure. Note the difference in hardness between the cell wall region and the centre of a cell in Material D. For Material A additional measurements were made in the Al_2O_3 and aluminium constituents using lower loads of 1 N and 0.05 N, respectively. The compressive strength was measured under displacement control at a crosshead speed of 8.3×10^{-7} m sec^{-1} on a Materials Testing System universal testing machine, using smooth WC–Co anvils to minimize barrelling due to frictional end effects. The specimens were cylindrical in shape with a diameter of 4.8 mm and length of 6.4 mm, giving a strain rate of $1.3 \times 10^{-4}\,sec^{-1}$. In all cases the length of the cylinders was parallel to the growth direction.

Figs 7, 8 and 9 show, respectively, the variation with temperature of the flexural strength σ_f, the fracture toughness K_{Ic}, and the critical strain energy release rate G_{Ic} of Materials A, B(iii) and D and of Durafrax® 1542. Each datum point represents a result obtained from a single specimen.

The flexural strength was measured in three-point bending on an Instron testing machine, using a span of 2.54 cm between the two outer supports of the test jig. These supports and the centre anvil were fixed; and each had a radius of curvature ~ 1 mm where it made contact with the specimen. The specimens were plates 1.6 mm thick, 5.5 mm wide and about 30 mm long. In each case the tensile surface was polished prior to testing on kerosene-soaked paper with a series of diamond pastes down to 1 μm in particle size. The tests were all performed at a crosshead speed of 8.3×10^{-7} m sec^{-1}. Since the composite plates were oriented perpendicular to the growth direction, the fracture propagated parallel to this direction. As the test temperature was raised above 1400 K Durafrax®

TABLE I Mechanical and physical properties of Materials A, B and D and of Durafrax® 1542

Property	Material					
	A	B(i)	B(ii)	B(iii)	D	Durafrax® 1542
Density ($kg\,m^{-3}$)	3530	3310	3040	2890	3610	3750
Thermal expansion ($10^{-6}\,K^{-1}$)	11.0	–	9.5	9.3	9.8	10.6
Thermal conductivity ($W\,m^{-1}\,K^{-1}$)	39.6	11.8	–	–	29.3	23.9
Young's modulus (GPa)	231 ± 3	121 ± 4	96	88 ± 1	304 ± 10	326 ± 4
Shear modulus (GPa)	88 ± 2	51	41	39	123 ± 4	132 ± 1
Poisson's ratio	0.312 ± 0.020	0.190 ± 0.037	0.184 ± 0.004	0.137 ± 0.006	0.240 ± 0.022	0.238 ± 0.014
Vickers hardness (GPa)	5.09 ± 0.26	1.82 ± 0.24	1.69 ± 0.32	1.41 ± 0.30	14.4 ± 0.7‡	14.6 ± 1.6
	17.3 ± 0.9*				8.22 ± 1.87§	
	0.525 ± 0.103†					
Compressive strength (MPa)	984 ± 85	414 ± 39	–	–	1910 ± 190	2420 ± 230

*Al_2O_3 region.
†Aluminium region.
‡Cell interior.
§Cell wall.

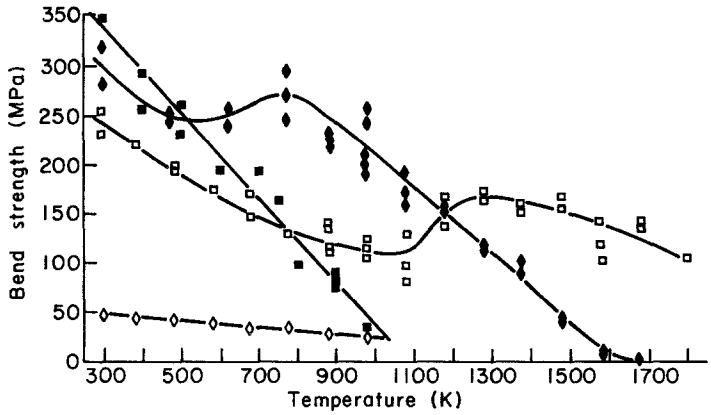

Figure 7 The variation of flexural strength with temperature for (■) Material A, (◇) Material B(iii), (□) Material D and (◆) Durafrax® 1542.

1542 exhibited increasingly non-linear stress–strain behaviour. In contrast, Materials A, B(iii) and D always exhibited linear behaviour.

At room temperature the flexural strength of Material B(iii) is 46 MPa. Additional tests show that, under the same conditions, the strengths of Materials B(i) and B(ii) are 43 and 44 MPa, respectively; and Brazilian diametral compression tests [59–62] of 3 mm diameter, 1 mm thick discs having their major surfaces perpendicular to the growth direction yield indirect tensile strengths of 24 and 22 MPa for these same composites. Evidently, the tensile strength of Material B is far less sensitive to microstructure than is hardness or Young's modulus. The lower tensile strength obtained from the Brazilian test may simply be due to the existence in the composite at failure of a compressive stress three times larger than the tensile stress [59]. This stress acts in the same plane as but perpendicular to the tensile stress. Alternatively, because the fracture propagated perpendicular to the growth direction in the Brazilian test, the lower strength may indicate that Material B exhibits significant anisotropy in its strength.

The plane-strain Mode I fracture toughness K_{Ic} was measured by the double torsion technique, using plate-shaped specimens 1.27 cm wide, 4.44 cm long and 1.6 mm thick. Each specimen had a centre groove 0.8 mm deep and 0.75 mm wide, and each was notched at the loading end of the groove to initiate fracture. In all cases, the crack ran along the groove. Since the plates were oriented perpendicular to the growth direction, fracture occurred parallel to this direction. The tests were carried out on the same Instron testing machine at the same crosshead speed of 8.3×10^{-7} m sec^{-1}, and the compliance was calculated from the dimensions of the specimen and the measured values of E and v. The critical strain energy release rate G_{Ic} was calculated at each temperature from the appropriate value of K_{Ic} and the measured *room temperature* values of E and v by the equation

$$G_{Ic} = \frac{K_{Ic}^2(1 - v^2)}{E} \quad (1)$$

Fig. 10 shows the residual flexural strength of Materials A, B(iii), and D and of Durafrax® 1542 following quenching from different temperatures T into water at room temperature (298 K). Again each datum point comes from a single specimen. The specimens were all 3.8 mm thick, 5.7 mm wide and 30 mm long. In each case the long axis was oriented perpendicular to the growth direction and the tensile surface was polished prior to quenching on kerosene-soaked paper with a series of diamond pastes down to 1 μm in particle size. All specimens were broken in three-point bending as described above.

4. Discussion

4.1. General

For a brittle material, strength, Young's modulus, and fracture toughness are all intimately related to the distribution of potential failure-initiating flaws in the material through Griffith's equations [63]. However, the nature of the relationship between each of these properties and the flaw distribution is quite different. Young's modulus depends on the broad features of the distribution; the fracture toughness is more sensitive to details of the distribution because cracks do not follow random paths but tend to seek out defects; and

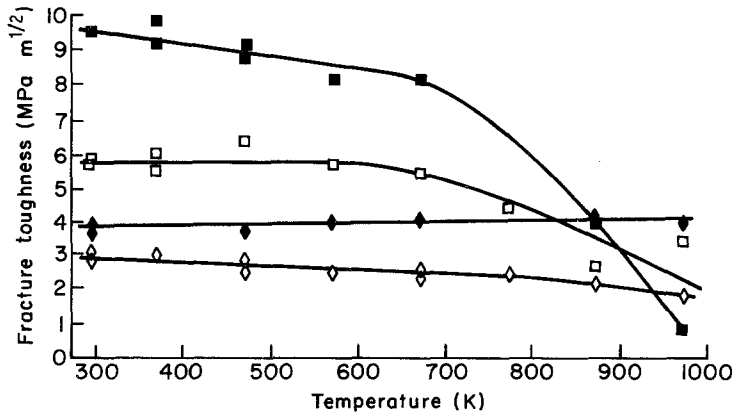

Figure 8 The variation of fracture toughness with temperature for (■) Material A, (◇) Material B(iii), (□) Material D and (◆) Durafrax® 1542.

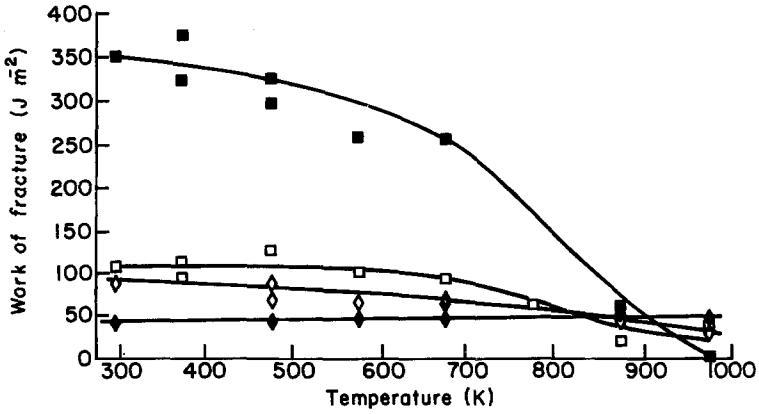

Figure 9 The variation of critical strain energy release rate with temperature for (■) Material A, (◇) Material B(iii), (□) Material D and (◆) Durafrax® 1542.

strength is critically dependent on the details of the extreme tail of the distribution at large flaw sizes. In tension or flexure, strength is generally determined by one single flaw. In compression several flaws are usually involved, although it is possible for failure to occur by propagation of a single flaw if the ratio of the applied principal stresses is less than or equal to zero – i.e. one principal stress falls to zero or becomes tensile [64]. This is likely to be the case in uniaxial compression when friction between the anvils and the ends of the specimen leads to barrelling.

4.2. Elastic constants

For Material A and Durafrax® 1542, the observed value of Young's modulus can be explained straightforwardly by combining the series (Reuss average) and/or parallel (Voigt average) rules for diphasic mixtures with a recent empirical treatment [65] of the influence of porosity. The series rule assumes the two phases to be laminates oriented perpendicular to an applied uniaxial stress, so that each carries the same stress. It gives

$$E = \frac{1}{(v_1/E_1) + (v_2/E_2)} \quad (2)$$

where the subscripts 1 and 2 refer to the two phases and E and v are Young's modulus and volume fraction, respectively. The parallel rule treats the two phases as laminates oriented parallel to an applied uniaxial stress, so that each undergoes the same strain. It leads to

$$E = E_1 v_1 + E_2 v_2 \quad (3)$$

Further, in the particular case of sintered Al_2O_3, Wang [65] found empirically that Young's modulus is related to the volume fraction p of porosity by

$$E = E_0 \exp[-(1.46p + 9.82p^2)] \quad (4)$$

where E_0 is the Young's modulus of fully dense material.

Because the ductile phase is continuous and the porosity randomly distributed in Material A, a valid approximation is to assume that (i) one half (11 vol %) of the aluminium (E = 70 GPa) [66] forms a parallel composite with the Al_2O_3 (E = 400 GPa) [66]; (ii) the other half forms a series composite with this parallel composite; and (iii) the porosity reduces the stiffness of this series composite according to Equation 4. This yields an estimate of 231 GPa for Young's modulus of Material A, in precise agreement with experiment. For Durafrax® 1542 the same model predicts E = 327 GPa when the Young's modulus of the grain boundary phase is assumed to be the same as that of soda–lime glass (70 GPa) [67]. Again, the agreement with experiment (326 GPa) is excellent.

In the case of Material D, equally good agreement between theory (307 GPa) and experiment (304 GPa) can be achieved by combining Equation 4 with Eshelby's theoretical treatment [68] of the effective Young's modulus E_{eff} of an elastic body containing a randomly distributed volume fraction v_2 of elastic spheres. This analysis gives

$$E_{eff} = \frac{9G_{eff}K_{eff}}{3K_{eff} + G_{eff}} \quad (5)$$

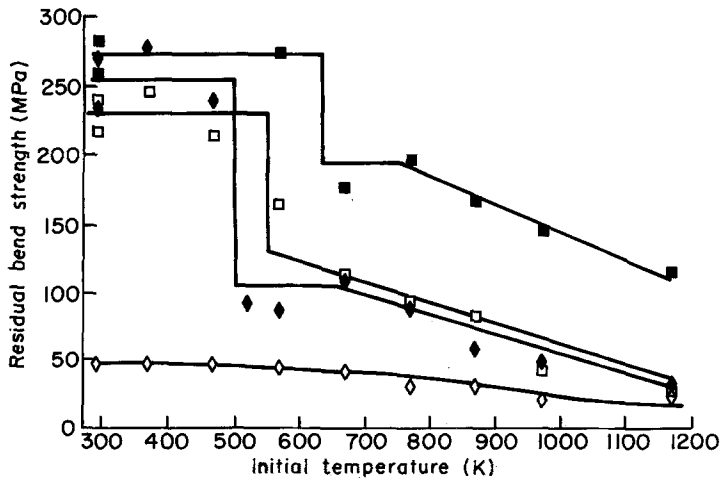

Figure 10 Residual flexural strength following quenching into water at 298 K as a function of initial temperature for (■) Material A, (◇) Material B(iii), (□) Material D and (◆) Durafrax® 1542.

where

$$K_{\text{eff}} = \frac{K_1}{1 + Av_2} \quad (6)$$

$$G_{\text{eff}} = \frac{G_1}{1 + Bv_2} \quad (7)$$

$$A = \frac{(K_1 - K_2)(4G_1 + 3K_1)}{K_1(4G_1 + 3K_2)} \quad (8)$$

$$B = \frac{G_2 - G_1}{\beta(G_1 - G_2) - G_1} \quad (9)$$

$$\beta = \frac{2(4 - 5\nu_1)}{15(1 - \nu_1)} \quad (10)$$

K and G denote the bulk modulus and the shear modulus, respectively, ν is Poisson's ratio, and the subscripts 1 and 2 refer to the matrix and the spheres, respectively.

Because of the tortuous shape and sometimes inhomogeneous distribution of the pores present in Material B, none of the available theoretical models provides a very good prediction of Young's modulus for this material. A further complication in this case is uncertainty about the volume fraction of aluminium present in the microstructure.

4.3. Hardness

The hardnesses of Durafrax® 1542 (14.6 GPa), the Al_2O_3 regions in Material A (17.3 GPa), and the interiors of the cells in Material D (14.4 GPa) are typical of the hardnesses reported for polycrystalline Al_2O_3 (12 to 23 GPa) [69–73]. This wide variation stems from such factors as experimental error, crystal orientation (plastic anisotropy), and, if the indentation is large compared to the characteristic dimensions of the microstructure, grain size and the possible presence of grain boundary phases. In the present work all high-load indentations had diagonals greater than the characteristic dimensions of the microstructures, though in Material D the diagonals were smaller than the diameter of the hexagonal cells.

The results for the different forms of Material B demonstrate that hardness falls rapidly with increase in porosity, from 1.82 GPa at a porosity of 0.16 to 1.41 GPa at a porosity of 0.26. It is also found that Material A is far harder than Material B, though both contain a similar volume fraction of Al_2O_3. This demonstrates that filling porosity with a second phase can considerably harden a two-phase composite, even if the second phase is significantly softer than the matrix. Qualitatively, the reason is that the presence of the second phase changes the nature of the irreversible deformation occurring beneath the indenter. Scanning electron microscopy showed that in the porous Material B the indentation formed primarily by localized compaction, while in the non-porous Material A it formed via plastic deformation at constant volume. The quantitative consequences of this change have been analysed by Yoffe [74], who has developed an analytical model of the indentation process which appears to succeed in describing both the elastic and the plastic stresses generated about an indentation in an essentially brittle (elastic) solid capable of only limited irreversible (plastic) deformation. Yoffe's model reveals that the elastic stresses constraining the irreversible deformation are greatly reduced when this deformation is accompanied by reduction in volume.

The low-load indentations made in the aluminium regions of Material A reveal that these are 2 to 3 times harder (Vickers hardness 0.525 GPa) than is usual for a fully annealed aluminium alloy [75]. The difference is tentatively attributed to enhanced constraint of the deformation occurring beneath the indenter by the surrounding Al_2O_3.

4.4. Compressive strength

The uniaxial compressive strength of Durafrax® 1542 is 2420 MPa. This value is not atypical of dense sintered alumina [76, 77], though it lies well below the maximum value of 4480 MPa reported by Rice [77]. Fractographic analysis is complicated by the adhesion of wear debris created by sliding of the opposing fracture surfaces over one another in the later stages of the fracture process, but it appears that the fracture is intergranular.

The low compressive strength of Material B(i) (414 MPa) stems from its irregular and interconnected pore structure, which provides both local stress concentrations to drive the crack and preferred paths for crack propagation. In this composite failure appears to be intragranular.

The twofold reduction in compressive strength, from 1910 to 984 MPa, between Materials D and A is striking given that the latter contains only about 50% more aluminium than the former. The difference stems from the different connectivities of the aluminium phase. Although it is weak in shear, the aluminium is effectively prevented from shearing in Material D by the fact that it is for the most part totally surrounded by Al_2O_3. In contrast, the interconnected aluminium present in Material A is less constrained as to its mode of deformation. Fractographic analysis shows that Material D fails by intragranular cracking of the Al_2O_3. The aluminium inclusions pull out and are smeared into plate-like debris during the final stages of fracture. The more extensive smearing of the higher volume fraction of (interconnected) aluminium present in Material A effectively obscures the fracture surface of this composite. Nevertheless, the fact that the surface is flat over distances large compared to the characteristic dimensions of the microstructure suggests that the Al_2O_3 matrix again fails in an intragranular fashion.

4.5. Flexural strength

The same difference in the constraint imposed on the ductile aluminium phase is reflected in the room-temperature flexural strength data. Material A is much stronger ($\sim$345 MPa) than Material D ($\sim$240 MPa) because the aluminium is better able to flow plastically and blunt failure-initiating flaws. So effective is this blunting mechanism that Material A is stronger than Durafrax 1542 ($\sim$300 MPa). In contrast, Material B(iii), which contains interconnected pores that serve as large flaws and only very little ductile aluminium to provide for blunting of the flaws, has a very low flexural strength ($\sim$45 MPa). Further reasons

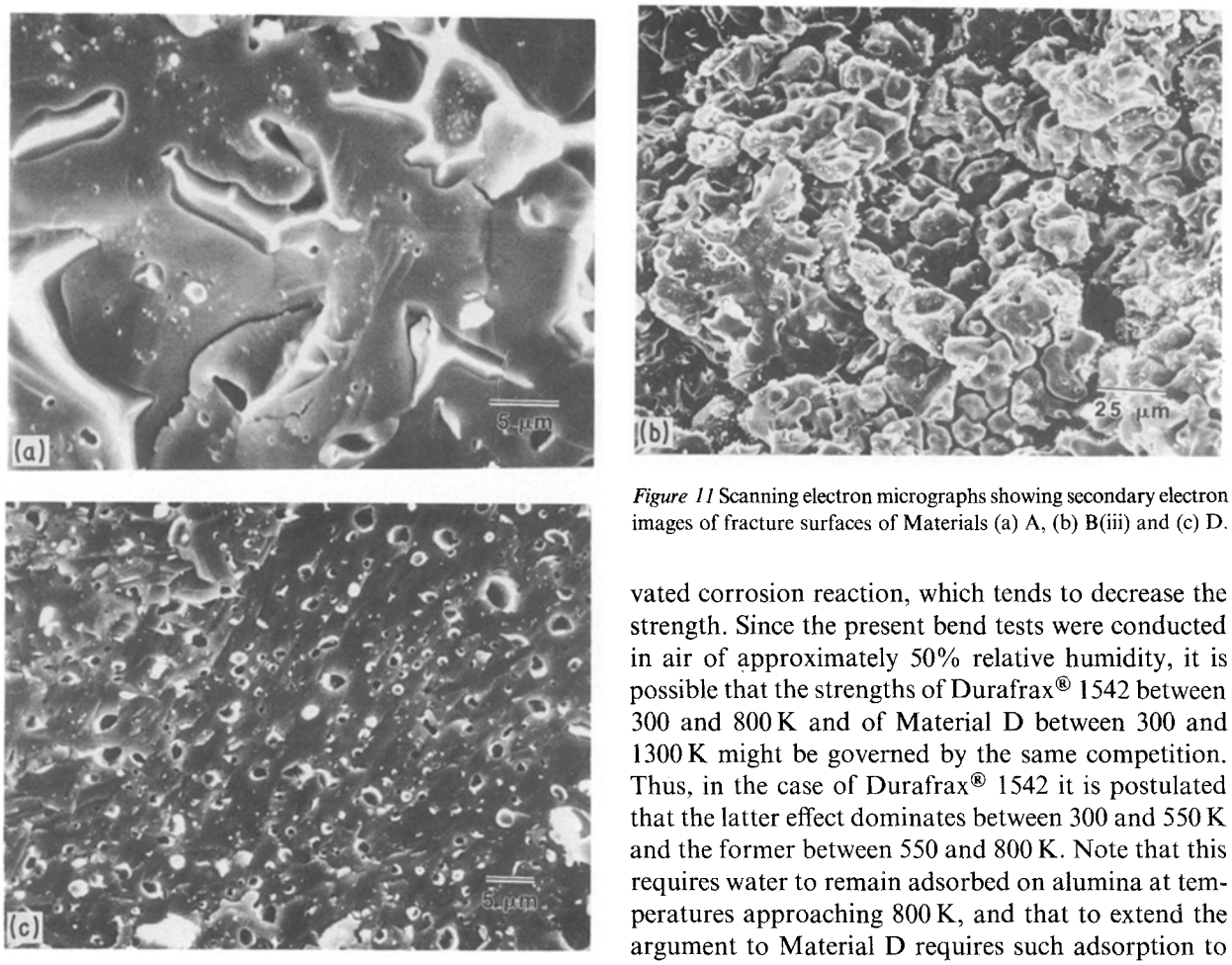

Figure 11 Scanning electron micrographs showing secondary electron images of fracture surfaces of Materials (a) A, (b) B(iii) and (c) D.

for the low strength of Material B(iii) are that this porosity provides local stress concentrations and an easy fracture path.

Material A, which contains the greatest volume fraction of aluminium, undergoes the greatest loss of flexural strength (from ~345 to ~35 MPa) as the temperature rises from 298 to 973 K, while the much weaker Material B(iii), which contains the least aluminium, loses little strength over the same temperature rise. The flexural strengths of Durafrax® 1542 and Material D exhibit similar behaviour of a more complex nature. That of Durafrax® 1542 falls from ~300 MPa at 300 K to ~250 MPa at 550 K, then rises slightly to ~275 MPa at 800 K before falling precipitously at higher temperatures – effectively to zero at 1700 K at the strain rate used in the present work. Similar behaviour has been reported by Spriggs *et al.* [78]. In like fashion, the flexural strength of Material D decreases more or less linearly from ~240 MPa at room temperature to ~110 MPa at 1100 K, then rises to ~170 MPa at 1300 K before falling slowly to ~105 MPa at 1800 K.

A variety of silicate glasses exhibit this same characteristic dependence of bend strength on temperature, although the maximum occurs at a lower temperature [79]. It is generally understood in terms of the stress corrosion model of slow crack growth proposed by Charles and Hillig [80, 81]. According to this model, raising the temperature causes two competing effects: (i) removal of the corrosive species (normally water) by thermal desorption, which tends to increase the strength; and (ii) acceleration of the thermally activated corrosion reaction, which tends to decrease the strength. Since the present bend tests were conducted in air of approximately 50% relative humidity, it is possible that the strengths of Durafrax® 1542 between 300 and 800 K and of Material D between 300 and 1300 K might be governed by the same competition. Thus, in the case of Durafrax® 1542 it is postulated that the latter effect dominates between 300 and 550 K and the former between 550 and 800 K. Note that this requires water to remain adsorbed on alumina at temperatures approaching 800 K, and that to extend the argument to Material D requires such adsorption to persist to ~1300 K.

Below ~900 K it is tempting to attribute the fall in strength of Material D with rise in temperature to thermal softening of the (isolated) regions of aluminium in the microstructure; but the lack of any discontinuity in the plot of bend strength against temperature at the melting point of aluminium argues against this, and it is difficult to see how further heating already molten aluminium could lead to the observed increase in strength between 1100 and 1300 K.

The fall in strength of Durafrax® 1542 as the test temperature rises above 800 K is attributed to softening of the glassy grain-boundary phase. Support for this view is provided by the results of parallel tests performed at a crosshead speed of 8×10^{-6} m sec^{-1} on a second, fully dense sintered alumina, Coors AD-998 (Coors Porcelain Co., Golden, Colorado). This material has a similar grain size and morphology to Durafrax® 1542, but it contains 99.8 wt % Al_2O_3 and correspondingly less SiO_2-based glass at its grain boundaries. Its strength is ~100 MPa at 1500 K and ~35 MPa at 1800 K. The corollary is that Material D retains almost half of its room-temperature strength at 1800 K because its clean grain boundaries (Fig. 5) reduce or eliminate grain boundary sliding.

4.6. Fractography

Figs 11a to c and Fig. 6 show fracture surfaces from bars of Materials A, B(iii) and D and of Durafrax® 1542 broken in three-point bending at room temperature. The mode of fracture is quite different in all four cases. Durafrax® 1542 fails in an intergranular manner (Fig. 6), whereas the three composites all fail in an

intragranular manner. Evidently, the clean grain boundaries in the latter materials are significantly stronger than the glass-filled grain boundaries in Durafrax® 1542. In Material A, the aluminium phase necks down to the chisel edge characteristic of ductile rupture, thereby contributing to the work of fracture via a crack bridging mechanism [53, 82]. The short length of the neck is evidence that the aluminium is strongly bonded to the Al_2O_3 [79]. At first sight, the fracture surface of Material B(iii) (Fig. 11b) exhibits surprisingly little evidence of fracture. This is because the crack propagates preferentially through the interconnected porosity and automatically selects a path of small load-bearing cross-section. On the rare occasions when the crack intersects aluminium inclusions these neck to points or chisel edges. Again the necks are short. In the case of Material D (Fig. 11c), the large majority of the aluminium inclusions pull out without contributing greatly to the work of fracture. It is suggested that this happens because (i) significant tensile stresses develop across the Al–Al_2O_3 interface during cooling from the growth temperature, and (ii) the aluminium inclusions are not of a sufficiently complex shape to prevent themselves from being pulled straight out of the cavities they occupy in the Al_2O_3 matrix if they cease to bond to it. The observation of some porosity at the Al–Al_2O_3 interface in polished cross-sections of Materials C and D (Fig. 4) is further evidence of the existence of appreciable interfacial stresses in these materials.

The possible causes of stress at the Al–Al_2O_3 interface are somewhat different in Materials A and D. In the former, the aluminium phase is fully interconnected in all three dimensions and the growth process does not run to completion. Thus, any tendency for the aluminium to shrink away from the Al_2O_3 and to generate tension across their common interface is probably accommodated at temperatures above 933 K by further infiltration of aluminium from the remaining reservoir of this metal. It is only the differential shrinkage on cooling from this temperature to room temperature that leads to tension across the Al–Al_2O_3 interface. Since the coefficients of linear thermal expansion of pure aluminium and Al_2O_3 are $\sim 30 \times 10^{-6}$ and $\sim 10 \times 10^{-6}\,K^{-1}$, respectively [83, 84], such shrinkage would amount to about 3% of the volume fraction of aluminium in the absence of any effects due to alloy elements. In the case of Material D, in which much of the aluminium is in the form of isolated inclusions, this shrinkage is augmented by (i) the contraction that occurs when aluminium solidifies and (ii) the differential shrinkage between molten aluminium and solid Al_2O_3 over the interval between the processing temperature (1600 K) and the melting point of aluminium (933 K). Since pure aluminium shrinks by 6% upon solidification [83] and the coefficient of linear thermal expansion of pure liquid aluminium is $\sim 41 \times 10^{-6}\,K^{-1}$ [83], these latter forms of shrinkage would amount to a further 13% of the volume fraction of aluminium in the absence of any effects due to alloy elements. Hence the total shrinkage in Material D could amount to ~16% of the volume fraction of aluminium, or about five times the possible shrinkage in Material A. This may be one important reason why aluminium pulls out during the fracture of Material D but necks to failure during fracture of Material A. The other important reason is the simpler morphology of the aluminium phase in Material D. In contrast to the continuous and tortuously shaped aluminium regions in Material A, the aluminium regions in Material D can fall straight out of their host Al_2O_3 matrix if they become debonded from it.

4.7. The ratio of compressive to tensile strength

Table II lists the ratio of the room-temperature compressive and flexural (tensile) strengths of Materials A, B(i), and D and of Durafrax® 1542. This ratio varies from unity for an ideal rigid plastic solid to ~8 for a linear elastic solid containing an arbitrarily oriented open crack of elliptic tip profile [85]. Table II thus shows that Durafrax® 1542 and Materials B(i) and D behave as essentially brittle solids, while Material A behaves in a manner that is partly ductile and partly brittle.

4.8. Fracture toughness and critical strain energy release rate

The value of $3.8\,MPa\,m^{1/2}$ obtained in the present work for the room-temperature fracture toughness K_{Ic} of Durafrax® 1542 is close to the average ($\sim 4\,MPa\,m^{1/2}$) of the many values reported in the literature [69, 72, 73, 86–88]. If E is taken as 326 GPa and ν as 0.238 (Table I), this yields a value of $42\,J\,m^{-2}$ for the critical strain energy release rate G_{Ic}. As expected [89], the porous composite B(iii), with its low aluminium content, exhibits a lower room-temperature fracture toughness of $2.9\,MPa\,m^{1/2}$. However, this material exhibits a higher value of G_{Ic} ($92\,J\,m^{-2}$) than does Durafrax® 1542 on account of its low Young's modulus (Equation 1). Larson *et al.* [90] also found porous forms of Al_2O_3 to have higher fracture energies than the fully dense form. They attributed the increase in fracture energy to secondary cracking during failure, but neither they nor the present authors succeeded in verifying this hypothesis. Materials D and A have room-temperature fracture toughnesses (5.9 and $9.5\,MPa\,m^{1/2}$, respectively) which are ~1.5× and ~2.5× greater than that of Durafrax® 1542. The corresponding values of G_{Ic} (110 and $350\,J\,m^{-2}$, respectively) exceed G_{Ic} for Durafrax® 1542 by factors of ~2.5× and ~8×. The latter increase is indicative of the considerable amount of energy absorbed by crack bridging [53, 82] during the failure of Material A (Fig. 11a). By comparison, crack bowing [17, 23, 48, 50, 51] – which Figs 11a and c suggest occurs in combination with crack bridging in Material A and

TABLE II Ratio at room temperature of compressive strength to flexural (tensile) strength

Material	Ratio
A	2.9
B(i)	9.6
D	8.0
Durafrax® 1542	8.1

TABLE III Values of the first, second and fifth thermal shock resistance parameters calculated from experimental data

Material	Parameter		
	R	R'	R''''
A	73.5	2.9	1.76×10^{-3}
B(iii)	34.9	0.41	4.51×10^{-3}
D	58.2	1.7	0.87×10^{-3}
Durafrax® 1542	55.6	1.3	0.30×10^{-3}

alone in Material D – leads to an appreciably smaller increase in K_{Ic} and G_{Ic}.

The increase in G_{Ic} resulting from crack bridging is roughly dependent on the product of three parameters – the volume fraction of the ductile phase and the failure stress and strain of this phase [82]. Since the failure stress of an aluminium alloy typically decreases more rapidly than its elongation to failure increases with rise in temperature [91], the contribution of crack bridging to G_{Ic} decreases at higher temperatures. It is for this reason that Material A exhibits the greatest variation of K_{Ic} and G_{Ic} with temperature (Figs 8 and 9). Conversely, Materials B(iii) and D exhibit little variation of K_{Ic} and G_{Ic} with temperature because they contain little or no ductile aluminium. Their fracture behaviour is governed by the brittle fracture energy of Al_2O_3, which is only a slowly varying function of temperature.

4.9. Thermal shock resistance

Table III lists the first, second, and fifth thermal shock resistance parameters [92]

$$R = \frac{\sigma_f(1 - \nu)}{E\alpha} \quad (11)$$

$$R' = \frac{k\sigma_f(1 - \nu)}{E\alpha} \quad (12)$$

$$R'''' = \frac{K_{Ic}^2}{\sigma_f^2(1 - \nu)} \quad (13)$$

as calculated from the room-temperature flexural strength σ_f and the data listed in Table I for Materials A, B(iii)* and D and for Durafrax® 1542; α is the coefficient of thermal expansion and k the thermal conductivity. Higher values of R and R' represent greater resistance to the initiation of fracture during rapid quenching and during steady-state heat flow down a steep temperature gradient; and higher values of R'''' indicate less crack propagation once the critical temperature drop ΔT_c necessary to initiate fracture is exceeded. R'''' is not, however, a wholly reliable indicator of the residual strength of a thermally fractured body because it measures only the total area of fracture surface created, and not the number and lengths of the individual cracks which account for this area.

R and R' both rank the test materials in the order A, D, Durafrax® 1542, B(iii), while R'''' ranks them in the order B(iii), A, D, Durafrax® 1542. The experimental data (Fig. 10) broadly confirm these rankings. Materials A and D and Durafrax® 1542 behave like a typical high-strength engineering ceramic [93]. For temperature drops $\Delta T < \Delta T_c$, pre-existing flaws do not extend and their residual strengths remain constant. However, when $\Delta T = \Delta T_c$, sudden rapid crack propagation occurs, leading to catastrophic loss of strength. In accord with the values of R and R', ΔT_c is largest for Material A and smaller for Durafrax® 1542 than for Material D. Further, the magnitude of the strength drop correlates with the calculated values of R''''. Theory predicts [93] that the long cracks which form are sub-critical in the stress field generated by the temperature drop ΔT_c, so ΔT must increase to ΔT_f before they begin to propagate again. As a result the residual strength is predicted to be independent of ΔT in the range $\Delta T_c < \Delta T < \Delta T_f$, and a short plateau should exist in the residual strength data for all three materials. This is observed for Material A and Durafrax® 1542. That it is not observed for Material D is probably due to insufficient data. As ΔT exceeds ΔT_f further crack growth is predicted to occur to a length that increases monotonically with increase in ΔT, resulting in a gradual decrease in residual strength, as observed. In contrast, Material B(iii) exhibits the gradual decrease in residual strength with increase in ΔT typical of a weaker ceramic [93]. The decrease is gradual because there is only a limited amount of elastic energy available in the quenched body when crack initiation occurs. This results in stable crack propagation to a final length that is a monotonically increasing function of ΔT. Consequently, the residual strength decreases monotonically with increase in ΔT (Fig. 10).

5. Conclusions

The novel Lanxide technology for the fabrication of Al_2O_3–Al composites has led to new materials with microstructures and combinations of properties different from those obtainable via conventional pressing and sintering or fusion casting methods. Further, the new process permits both microstructure and properties to be varied widely in a controllable manner. In particular, it is possible to obtain useful gains over typical dense sintered aluminas in low-temperature toughness, tensile strength and thermal shock resistance at only modest cost in loss of hardness, stiffness, and compressive strength. Alternatively, it is possible to obtain modest gains in toughness and more significant gains in high-temperature bend strength while maintaining room-temperature values of hardness, stiffness, and compressive strength close to those characteristic of a dense sintered alumina.

References

1. S. M. WIEDERHORN, *Ann. Rev. Mater. Sci.* **14** (1984) 373.
2. K. T. FABER, *Ceram. Eng. Sci. Proc.* **5** (1984) 408.
3. A. G. EVANS, *Mater. Sci. Eng.* **71** (1985) 3.
4. R. W. DAVIDGE, *Phil. Trans. R. Soc.* **A310** (1983) 113.
5. R. W. RICE, *J. Phys. Chem. Solids* **45** (1984) 1033.
6. F. KERKHOF, *Interceram (Suppl.)* **32** (1983) 1.
7. A. G. EVANS, A. H. HEUER and D. L. PORTER, in "Advances in Research on the Strength and Fracture of

*k was actually measured for B(i) rather than B(iii), but the difference is not expected to be significant.

Materials", Vol. 1, edited by D. M. R. Taplin (Pergamon, Oxford, 1977) p. 529.
8. A. G. EVANS, in "Microstructure and Properties of Ceramic Materials", edited by T. S. Yen and J. A. Pask (Science Press, Beijing, 1984) p. 236.
9. M. R. PIGGOTT, "Load Bearing Fibre Composites" (Pergamon, Oxford, 1980) p. 211.
10. A. KELLY, in "Frontiers in Materials Science", edited by L. E. Murr and C. Stein (Dekker, New York, 1976) p. 335.
11. D. C. PHILLIPS, in "Handbook of Composites", Vol. 4, edited by A. Kelly and Y. N. Rabotnov (Elsevier, Amsterdam, 1983) p. 373.
12. R. W. RICE, C. V. MATT, W. J. McDONOUGH, K. R. McKINNEY and C. C. WU, *Ceram. Eng. Sci. Proc.* **3** (1982) 698.
13. B. A. BENDER, D. LEWIS III, W. S. COBLENZ and R. W. RICE, *ibid.* **5** (1984) 513.
14. G. JINGKUN and T. S. YEN, in "Microstructure and Properties of Ceramic Materials", edited by T. S. Yen and J. A. Pask (Science Press, Beijing, 1984) p. 281.
15. D. T. RANKIN, J. J. STIGLICH, D. R. PETRAK and R. RUH, *J. Amer. Ceram. Soc.* **54** (1971) 277.
16. D. J. GREEN, P. S. NICHOLSON and J. D. EMBURY, in "Advances in Research on the Strength and Fracture of Materials", Vol. 3, edited by D. M. R. Taplin (Pergamon, Oxford, 1977) p. 941.
17. *Idem, J. Mater. Sci.* **14** (1979) 1413.
18. P. HING and G. W. GROVES, *ibid.* 7 (1972) 427.
19. C. O. McHUGH, T. J. WHALEN and M. J. HUMENIK, *J. Amer. Ceram. Soc.* **49** (1966) 486.
20. Y. NIVAS and R. M. FULRATH, *ibid.* **53** (1970) 188.
21. M. A. STETT and R. M. FULRATH, *ibid.* **51** (1968) 599.
22. V. D. KRSTIC, P. S. NICHOLSON and R. G. HOAGLAND, *ibid.* **64** (1981) 499.
23. F. F. LANGE, *ibid.* **54** (1971) 614.
24. N. MIYATA, K. TANIGANA and H. JINNO, in "Fracture Mechanics of Ceramics", Vol. 5, edited by R. C. Bradt, A. G. Evans, D. P. H. Hasselman and F. F. Lange (Plenum, New York, 1983) p. 609.
25. D. P. H. HASSELMAN and R. M. FULRATH, *J. Amer. Ceram. Soc.* **49** (1966) 68.
26. R. W. RICE, *J. Mater. Sci.* **19** (1984) 1267.
27. R. W. RICE, S. W. FREIMAN and J. J. MECHOLSKY Jr, *J. Amer. Ceram. Soc.* **63** (1980) 129.
28. J. J. MECHOLSKY, in "Fracture Mechanics of Ceramics", Vol. 6, edited by R. C. Bradt, A. G. Evans, D. P. H. Hasselman and F. F. Lange (Plenum, New York, 1983) p. 165.
29. R. W. RICE, S. W. FREIMAN and P. F. BECHER, *J. Amer. Ceram. Soc.* **64** (1981) 345.
30. R. W. RICE and S. W. FREIMAN, *ibid.* **64** (1981) 350.
31. P. BOCH and J. C. GLANDUS, *Interceram* **32** (1983) 33.
32. *Idem, ibid.* **33** (1984) 37.
33. V. D. KRSTIC, *Acta Metall.* **33** (1985) 521.
34. R. W. DAVIDGE, in "Fracture Mechanics of Ceramics", Vol. 2, edited by R. C. Bradt, D. P. H. Hasselman and F. F. Lange (Plenum, New York, 1974) p. 447.
35. L. A. SIMPSON, in "Fracture Mechanics of Ceramics", Vol. 2, edited by R. C. Bradt, D. P. H. Hasselman and F. F. Lange (Plenum, New York, 1974) p. 567.
36. I. J. McCOLM, "Ceramic Science for Materials Technologists" (Blackie, Glasgow, 1983) p. 272.
37. F. F. LANGE, in "Microstructure and Properties of Ceramic Materials", edited by T. S. Yen and J. A. Pask (Science Press, Beijing, 1984) p. 261.
38. E. P. BUTLER, *Mater. Sci. Tech.* **1** (1985) 417.
39. N. CLAUSSEN, in "Ceramics in Advanced Energy Technologies", edited by H. Krockel, M. Merz and O. van der Biest (Reidel, Dordrecht, 1982) p. 51.
40. R. STEVENS and P. A. EVANS, *Br. Ceram. Trans. J.* **83** (1984) 28.
41. Y. FU and A. G. EVANS, *Acta Metall.* **33** (1985) 1515.
42. A. G. EVANS and Y. FU, *ibid.* **33** (1985) 1525.
43. N. CLAUSSEN, J. STEEB and R. F. PABST, *J. Amer. Ceram. Soc.* **56** (1977) 559.
44. D. J. GREEN, P. S. NICHOLSON and J. D. EMBURY, *ibid.* **56** (1973) 619.
45. K. T. FABER, A. G. EVANS and M. D. DRORY, in "Fracture Mechanics of Ceramics", Vol. 6, edited by R. C. Bradt, A. G. Evans, D. P. H. Hasselman and F. F. Lange (Plenum, New York, 1983) p. 77.
46. J. SELSING, *J. Amer. Ceram. Soc.* **44** (1961) 419.
47. F. F. LANGE, in "Fracture Mechanics of Ceramics", Vol. 4, edited by R. C. Bradt, D. P. H. Hasselman and F. F. Lange (Plenum, New York, 1978) p. 799.
48. *Idem, Phil. Mag.* **22** (1970) 983.
49. S. B. BHADURI, *J. Mater. Sci. Lett.* **4** (1985) 954.
50. D. J. GREEN, *J. Amer. Ceram. Soc.* **66** (1983) C4.
51. D. J. GREEN and P. S. NICHOLSON, in "Fracture Mechanics of Ceramics", Vol. 4, edited by R. C. Bradt, D. P. H. Hasselman and F. F. Lange (Plenum, New York, 1978) p. 945.
52. J. C. SWEARENGEN, E. K. BEAUCHAMP and R. J. EAGAN, in "Fracture Mechanics of Ceramics", Vol. 4, edited by R. C. Bradt, D. P. H. Hasselman and F. F. Lange (Plenum, New York, 1978) p. 937.
53. D. J. GREEN, P. S. NICHOLSON and J. D. EMBURY, *J. Mater. Sci.* **14** (1979) 1657.
54. M. S. NEWKIRK, A. W. URQUHART, H. R. ZWICKER and E. BREVAL, *J. Mater. Res.* **1** (1986) 81.
55. T. ALLEN, "Particle Size Measurement", 3rd Edn (Chapman & Hall, London, 1981) p. 568.
56. R. E. NEWNHAM, D. P. SKINNER and L. E. CROSS, *Mater. Res. Bull.* **13** (1978) 525.
57. H. E. EXNER and H. P. HOUGARDY, "Quantitative Analysis of Microstructures" (Deutsche Gesellschaft für Metallkunde, Oberursel, 1983).
58. S. SPINNER and W. E. TEFFT, *ASME Proc.* **61** (1961) 1221.
59. J. C. JAEGER and N. G. W. COOK, "Fundamentals of Rock Mechanics" (Chapman & Hall, London, 1971) p. 160, 245.
60. R. H. MARION and J. K. JOHNSTONE, *Bull. Amer. Ceram. Soc.* **56** (1977) 998.
61. O. VARDAR and I. FINNIE, *Int. J. Fracture* **11** (1975) 495.
62. M. M. MELLOR and I. HAWKES, *Eng. Geol.* **5** (1971) 173.
63. A. A. GRIFFITH, *Phil. Trans. R. Soc.* **A221** (1920) 163.
64. E. HOEK and Z. T. BIENIAWSKI, *Int. J. Fracture* **26** (1984) 276.
65. J. C. WANG, *J. Mater. Sci.* **19** (1984) 809.
66. G. SIMMONS and H. WANG, "Single Crystal Elastic Constants and Calculated Aggregate Properties" (MIT Press, Cambridge, Massachusetts, 1971) p. 4, 146.
67. D. C. BOYD and D. A. THOMPSON, "Kirk Othmer: Encyclopedia of Chemical Technology", 3rd Edn, Vol. 11 (Wiley, New York, 1980) p. 807.
68. J. D. ESHELBY, *Proc. R. Soc.* **A241** (1957) 376.
69. G. R. ANSTIS, P. CHANTIKUL, B. R. LAWN and D. B. MARSHALL, *J. Amer. Ceram. Soc.* **64** (1981) 533.
70. B. R. LAWN and V. R. HOWES, *J. Mater. Sci.* **16** (1981) 2745.
71. D. B. MARSHALL, T. NOMA and A. G. EVANS, *J. Amer. Ceram. Soc.* **65** (1982) C175.
72. B. R. LAWN and D. B. MARSHALL, *ibid.* **62** (1979) 347.
73. J. LANKFORD, *J. Mater. Sci.* **17** (1982) 493.
74. E. H. YOFFE, *Phil. Mag.* **A46** (1982) 617.
75. D. TABOR, "Hardness of Metals" (Oxford University Press, Oxford, 1951) p. 166.
76. F. P. KNUDSEN, *J. Amer. Ceram. Soc.* **42** (1959) 376.
77. R. W. RICE, in "Ceramics in Severe Environments", edited by W. W. Kriegel and H. Palmour III (Plenum, New York, 1971) p. 195.
78. R. M. SPRIGGS, J. B. MITCHELL and T. VASILOS, *J. Amer. Ceram. Soc.* **47** (1964) 323.
79. A. KELLY and N. H. MacMILLAN, "Strong Solids", 3rd Edn (Oxford University Press, Oxford, 1986) p. 159.
80. R. J. CHARLES and W. B. HILLIG, in Proceedings of

Symposium on the Mechanical Strength of Glass and Ways of Improving It, Florence, September, 1961 (Union Scientifique Continentale du Verre, Charleroi, Belgium, 1962) p. 511.
81. W. B. HILLIG and R. J. CHARLES, in "High Strength Materials", edited by V. F. Zackay (Wiley, New York, 1965) p. 682.
82. S. KUNZ-DOUGLASS, P. W. R. BEAUMONT and M. F. ASHBY, *J. Mater. Sci.* **15** (1980) 1109.
83. A. R. UBBELOHDE, "The Molten State of Matter" (Wiley, New York, 1978) p. 239.
84. W. D. KINGERY, H. K. BOWEN and D. R. UHLMANN, "Introduction to Ceramics", 2nd Edn (Wiley, New York, 1976) p. 593.
85. A. A. GRIFFITH, in Proceedings of 1st International Congress on Applied Mechanics, edited by Biezeno and Burgers (Technische Boekhandel and Drukkerij J. Waltman Jr, Delft, 1925) p. 55.
86. R. F. COOK and B. R. LAWN, *J. Amer. Ceram. Soc.* **66** (1983) C200.
87. L. M. BARKER, ASTM STP 678 (American Society for Testing and Materials, Philadelphia, 1979) p. 73.
88. P. CHANTIKUL, G. R. ANSTIS, B. R. LAWN and D. B. MARSHALL, *J. Amer. Ceram. Soc.* **64** (1981) 539.
89. K. KENDALL, in "Physics and Chemistry of Porous Media", edited by D. L. Johnson and P. N. Sen (American Institute of Physics, New York, 1984) p. 79.
90. D. R. LARSON, J. A. COPPOLA, D. P. H. HASSELMAN and R. C. BRADT, *J. Amer. Ceram. Soc.* **57** (1974) 417.
91. "Aluminum Standards and Data 1984", 8th Edn (Aluminum Association, Washington, DC, 1984) p. 33.
92. J. NAKAYAMA, in "Fracture Mechanics of Ceramics", Vol. 2, edited by R. C. Bradt, D. P. H. Hasselman and F. F. Lange (Plenum, New York, 1974) p. 759.
93. R. W. DAVIDGE, "Mechanical Behaviour of Ceramics" (Cambridge University Press, Cambridge, England, 1979) p. 118.

Received 9 November 1987
and accepted 1 March 1988